Nonlinear Dyn (2019) 97:663–677
https://doi.org/10.1007/s11071-019-05005-6

ORIGINAL PAPER

Analytical analysis of the vibrational tristable energy harvester with a RL resonant circuit

Dongmei Huang · Shengxi Zhou · Grzegorz Litak

Received: 30 November 2018 / Accepted: 7 May 2019 / Published online: 16 May 2019

Abstract In this paper, analytical analysis of the vibrational tristable energy harvester with a RL resonant circuit is presented. The analytical solutions of the steady-state response displacement and the steady-state output voltage are derived via the method of multiple scales. The influence mechanism of the excitation amplitude and frequency, the electromechanical coupling coefficient, the damping and the detuning parameters on the dynamic response characteristics and the output voltage is studied. In order to enhance the energy harvesting performance, the appropriate choice of the excitation amplitude and the electromechanical coupling coefficient is discussed.

Keywords Tristable · Vibration · Energy harvesting · Nonlinear · Resonant circuit

1 Introduction

Recently, nonlinear vibration energy harvesting has become a research hot spot, because it owns a very good application potential for solving the challenging issue of energy supply for embedded wireless sensors and portable electromechanical devices [1,2]. The main advantage of nonlinear energy harvesters over traditional linear energy harvesters is their wide operating frequency range, which benefits for energy harvesting from frequency broadband vibrations [3–5]. It is well known that an uncertain factor which is inevitably existing may influence the frequency and level of ambient excitation vibrations. This stimulates researchers to design suitable broadband nonlinear energy harvesters [6,7].

For the bistable energy harvesters (BEH) under random base excitations, the dynamic response mechanism and enhanced energy harvesting were numerically and experimentally verified by Cottone et al. [8] and Litak et al. [9,10]. Under harmonic base excitations, the high-energy interwell oscillations of the BEH were classified and defined by Erturk and Inman [11], which lead to large-amplitude output voltage and enhance energy harvesting. Zhou et al. [12] numerically and experimentally obtained the high-energy interwell oscillation frequency range of the BEH in a magnetic-coupled rotatable energy harvesting structure under frequency-swept excitations. Stanton et al. [13] developed a theoretical model of the magnetic-coupled BEH to predict the nonlinear response characteristics and the energy harvesting performance. Fotsa and Woafo [14] demonstrated the chaotic response of the BEH under some excitation conditions. These characteristics

D. Huang
School of Mathematics and Statistics, Xidian University, Xi'an 710071, Shaanxi, China

D. Huang· S. Zhou (✉)
School of Aeronautics, Northwestern Polytechnical University, Xi'an 710072, China
e-mail: zhoushengxi@nwpu.edu.cn

G. Litak
Department of Automation, Lublin University of Technology, Nadbystrzycka 36, 20-618 Lublin, Poland

were also found in bidirectional and plate-based BEHs [15,16]. It was found that the high-energy oscillations in the multisolution range of the BEH are difficult to realize under zero initial conditions [17,18]. Meanwhile, the high-branch oscillations of nonlinear monostable energy harvesters [19,20] and internal resonance-based nonlinear energy harvesters with zero initial conditions [21,22] are also expected but difficult to realize under constant frequency excitations.

Zhou et al. [23] designed a vibrational tristable energy harvester (TEH) for the purpose of improving energy harvesting performance under low-level ambient vibrations. TEHs were numerically and experimentally verified: they have better energy harvesting performance when compared with their bistable counterparts under low-level harmonic or random excitations [23–25]. In order to explore the influence of material properties of the TEH, Tékam et al. [26] and Kwuimy et al. [27] numerically presented the energy harvesting performance of a TEH with fractional-order viscoelastic material. The complete parameter influence mechanism of TEHs was explored by Panyam et al. [28] and Zhou et al. [29]. It is found that the effective working frequency range and interwell oscillations of the TEH are impossible to perform when the constant frequency excitation level is very low. This demonstrates that above-mentioned nonlinear energy harvesters have their expected performance enhancement only when they vibrate at the higher orbits. However, with zero initial conditions, the nonlinear energy harvesters usually follow the low-energy orbits, which will result in small-amplitude voltage output.

To solve this issue, Zhou et al. [30] presented an initial impact method to facilitate nonlinear vibrational energy harvesters to overcome their potential barriers and achieve high-energy oscillations under low-level excitations. Based on this method, the effective bandwidths of the BEH and the TEH were experimentally increased to 15 Hz and 12 Hz from 3 Hz and 5 Hz, respectively. Later on, Mallicket et al. [31] presented an electronic control method to switch to the high-energy orbit of a vibrational nonlinear energy harvester. They claimed that this method can improve the energy harvesting performance over a wide frequency range under frequency–amplitude-varying excitations. Lan et al. [32] introduced a voltage impulse perturbation approach via a negative resistance to induce high-energy oscillations of vibrational nonlinear energy harvesters. Multiple solutions were discussed by Syta et al. [33], and consequently their robust and adaptive control was proposed by Haji et al. [34]. The above-mentioned methods can improve the energy harvesting performance of nonlinear vibrational energy harvesters by inducing high-energy oscillations in the multisolution range. However, these methods are active methods which need additional energy input. Taking a different approach, Yan et al. [35] presented a passive method that a resonant circuit was connected with the TEH. The energy harvesting enhancement was numerically verified.

This paper theoretically analyzes the response mechanism of the TEH with the resonant circuit to enhance vibration energy harvesting performance. In Sect. 2, the theoretical analysis of the TEH with the RL resonant circuit is presented. Then, in order to understand the energy performance of the harvester in detail, the effects of the relative parameters on the TEH are considered in Sect. 3. Lastly, the main conclusions are given.

2 System description and theoretical analysis

Figure 1 presents the schematic diagram of the TEH with the RL resonant circuit [35]. Because of the nonlinear magnetic force, the TEH owns five equilibrium positions ($-x_2$ and x_2 are unstable equilibrium positions, while $-x_1$, 0 and x_1 are stable equilibrium positions). The nonlinear magnetic force can be experimentally measured or numerically calculated [13,14,23]. In addition, a load resistance R and an electrical inductance L make up a resonant circuit connected to the TEH.

The governing equation for the mechanical motion of the TEH is usually expressed as [23,35]:

$$m\ddot{x}(t) + c\dot{x}(t) + F_r - \theta_p \upsilon(t) = F(t) \tag{1}$$

where m, c and k, respectively, stand for the equivalent mass, the equivalent damping and the equivalent stiffness of the harvester. θ_p is the equivalent electromechanical coupling coefficient, which mainly depends on the piezoelectric material. $\upsilon(t)$ is the voltage generated by the piezoelectric material. F_r is the equivalent nonlinear restoring force, which is made up of external magnetic force and equivalent linear restoring force. $F(t)$ is the equivalent excitation force.

The dimensional expression of Eq. (1) is:

$$\ddot{x}(t) + 2\zeta\omega\dot{x}(t) + f_r - \theta\upsilon(t) = f\sin(\Omega t) \tag{2}$$

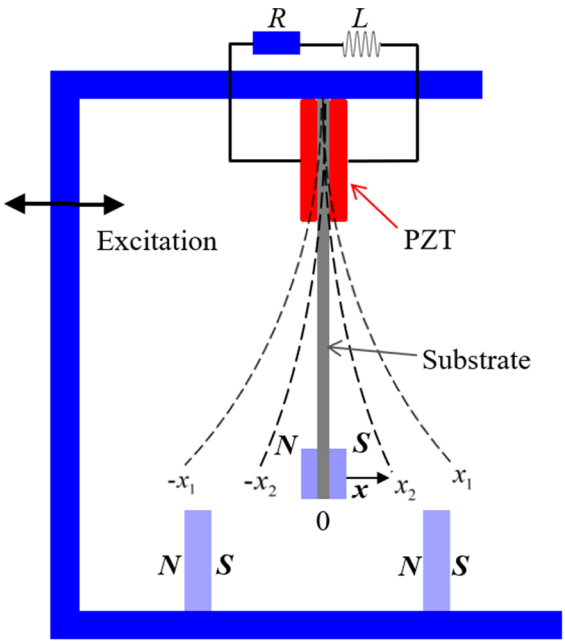

Fig. 1 Schematic of the TEH with a RL resonant circuit. $-x_1$, 0, x_1 denote the stable while $-x_2$, x_2 unstable equilibria

where ζ is the dimensionless damping ratio. θ is the dimensionless electromechanical coupling coefficient. ω is the equivalent natural frequency of the TEH. Ω is the angular excitation frequency. $f\sin(\Omega t)$ is the external excitation. x is the displacement of the TEH with respect to the base. $f_r = \frac{\omega^2 x}{x_1^2 x_2^2}(x^2 - x_1^2)(x^2 - x_2^2)$ is the dimensional nonlinear restoring force, where ω^2 is the first-order stiffness coefficient and x_1 and x_2 are the distance of the nonzero equilibrium position to the zero equilibrium position.

Then, Eq. (2) could be rewritten as:

$$\ddot{x}(t) + 2\zeta\omega\dot{x}(t) + \omega^2 x(t) + a_1 x^3(t) + a_2 x^5(t) - \theta\upsilon(t) = f\sin(\Omega t) \tag{3}$$

where a_1 and a_2 are the coefficients of the nonlinear stiffness terms.

The governing equation for the electrical response of the TEH is shown as [35,36]:

$$C_p\dot{\upsilon}(t) + \theta\dot{x}(t) + \frac{\upsilon(t) - L\dot{I}_L}{R} = 0 \tag{4}$$

where I_L is the current flows in the load circuit represented by:

$$I_L = -C_p\dot{\upsilon}(t) - \theta\dot{x}(t) \tag{5}$$

Thus, the final dimensional governing equations of the TEH can be obtained [35,36]:

$$\ddot{x}(t) + 2\zeta\omega\dot{x}(t) + \omega^2 x(t) + a_1 x^3(t) + a_2 x^5(t) - \theta\upsilon(t) = f\sin(\Omega t) \tag{6}$$

$$\ddot{\upsilon}(t) + 2\zeta_e\omega_e\dot{\upsilon}(t) + \omega_e^2\upsilon(t) + m_e\ddot{x}(t) + c_e\dot{x}(t) = 0 \tag{7}$$

where $\zeta_e = \frac{R}{2\omega_e L}$; $\omega_e^2 = \frac{1}{LC_p}$; $m_e = \frac{\theta}{C_p}$; $c_e = R\theta\omega_e^2$.

Then, the generated voltage across the end of the electrical resistance R can be expressed as,

$$\upsilon_R = I_L R = -\frac{2\zeta_e}{\omega_e}\dot{\upsilon} - \frac{c_e}{\omega_e^2}\dot{x} \tag{8}$$

In order to utilize the method of multiple scales [37–39], the small parameters are introduced as follows:

$$\zeta = \varepsilon\hat{\zeta}, a_1 = \varepsilon\hat{a}_1, a_2 = \varepsilon\hat{a}_2, \quad \theta = \varepsilon\hat{\theta}, f = \varepsilon\hat{f}, \quad \zeta_e = \varepsilon\hat{\zeta}_e, m_e = \varepsilon\hat{m}_e, \quad c_e = \varepsilon\hat{c}_e \tag{9}$$

Then, Eqs. (6) and (7) can be expressed as:

$$\ddot{x}(t) + 2\varepsilon\hat{\zeta}\omega\dot{x}(t) + \omega^2 x(t) + \varepsilon\hat{a}_1 x^3(t) + \varepsilon\hat{a}_2 x^5(t) - \varepsilon\hat{\theta}\upsilon(t) = \varepsilon\hat{f}\sin(\Omega t) \tag{10}$$

$$\ddot{\upsilon}(t) + 2\varepsilon\hat{\zeta}_e\omega_e\dot{\upsilon}(t) + \omega_e^2\upsilon(t) + \varepsilon\hat{m}_e\ddot{x}(t) + \varepsilon c_e\dot{x}(t) = 0 \tag{11}$$

According to the method of multiple scales, the approximate solutions of $x(t)$ and $\upsilon(t)$ are expressed as:

$$x(t,\varepsilon) = x_0(T_0, T_1) + \varepsilon x_1(T_0, T_1) + \cdots \tag{12}$$

$$\upsilon(t,\varepsilon) = \upsilon_0(T_0, T_1) + \varepsilon\upsilon_1(T_0, T_1) + \cdots \tag{13}$$

where $T_0 = t$ is a fast time scale, $T_1 = \varepsilon t$ is the slow time scale.

By denoting the differential operators $D_0 = \partial/\partial T_0$, $D_1 = \partial/\partial T_1$ and using the following differential operators, we can obtain:

$$\frac{\mathrm{d}}{\mathrm{d}t} = D_0 + \varepsilon D_1 + \cdots \tag{14}$$

$$\frac{\mathrm{d}^2}{\mathrm{d}t^2} = D_0^2 + 2\varepsilon D_0 D_1 + \varepsilon^2(D_1^2 + 2D_0 D_2) + \cdots \tag{15}$$

Substituting Eqs. (12–15) into Eqs. (10) and (11), it is easy to obtain:

$$D_0^2 x_0(T_0, T_1) + \omega^2 x_0(T_0, T_1) = 0 \tag{16}$$

$$D_0^2 x_1(T_0, T_1) + \omega^2 x_1(T_0, T_1) = -2D_0 D_1 x_0 - 2\hat{\zeta}\omega D_0\upsilon_0 - \hat{a}_1 x_0^3 - \hat{a}_2 x_0^5 + \hat{\theta}\upsilon_0 + \hat{f}\sin(\Omega t) \tag{17}$$

$$D_0^2 \upsilon_0(T_0, T_1) + \omega_e^2 \upsilon_0(T_0, T_1) = 0 \tag{18}$$

$$\begin{aligned} &D_0^2 \upsilon_1(T_0, T_1) + \omega_e^2 \upsilon_1(T_0, T_1) \\ &\quad = -2D_0 D_1 \upsilon_0 - 2\hat{\xi}_e \omega_e D_0 \upsilon_0 - \hat{m}_e D_0^2 x_0 \\ &\qquad - \hat{c}_e D_0 x_0 \end{aligned} \tag{19}$$

The general solutions of Eqs. (16) and (18) can be expressed as:

$$x_0(T_0, T_1) = a(T_1)\exp(i\omega T_0) + cc \tag{20}$$

$$\upsilon_0(T_0, T_1) = b(T_1)\exp(i\omega_e T_0) + cc \tag{21}$$

where cc denotes the complex conjugate. $a(T_1)$ and $b(T_1)$ denote the slowly varying amplitude of the response.

Substituting Eqs. (20) and (21) to Eqs. (17) and (19), we can obtain the following equations:

$$\begin{aligned} &D_0^2 x_1 + \omega^2 x_1 \\ &\quad = -2D_0 D_1 (a(T_1)\exp(i\omega T_0) + cc) \\ &\qquad - 2\hat{\xi}\omega D_0 (a(T_1)\exp(i\omega T_0) + cc) \\ &\qquad - \hat{a}_1 (a(T_1)\exp(i\omega T_0) + cc)^3 \\ &\qquad - \hat{a}_2 (a(T_1)\exp(i\omega T_0) + cc)^5 \\ &\qquad + \hat{\theta}(b(T_1)\exp(i\omega_e T_0) + cc) \\ &\qquad + \frac{\hat{f}}{2i}(\exp(i\Omega T_0) - cc) \end{aligned} \tag{22}$$

$$\begin{aligned} &D_0^2 \upsilon_1 + \omega_e^2 \upsilon_1 \\ &\quad = -2D_0 D_1 (b(T_1)\exp(i\omega_e T_0) + cc) \\ &\qquad - 2\hat{\xi}_e \omega_e D_0 (b(T_1)\exp(i\omega_e T_0) + cc) \\ &\qquad - \hat{m}_e D_0^2 (a(T_1)\exp(i\omega T_0) + cc) \\ &\qquad - \hat{c}_e D_0 (a(T_1)\exp(i\omega T_0) + cc) \end{aligned} \tag{23}$$

To investigate the primary resonance of governing equations (10) and (11), the detuning parameters σ and σ_1 are introduced such that $\Omega = \omega + \varepsilon\sigma$ and $\omega_e = \omega + \varepsilon\sigma_1$ and the 1:1 internal resonance is considered.

The secular terms of Eqs. (22) and (23) can be neglected if:

$$\begin{aligned} &-2i\omega a'(T_1) - 2\hat{\zeta} i\omega^2 a(T_1) \\ &\quad - 3\hat{a}_1 a^2(T_1)\bar{a}(T_1) - 10\hat{a}_2 a^3(T_1)\bar{a}^2(T_1) \\ &\quad + \hat{\theta} b(T_1)\exp(i\sigma_1 T_1) + \frac{\hat{f}}{2i}\exp(i\sigma T_1) = 0 \end{aligned} \tag{24}$$

$$\begin{aligned} &-2i\omega_e b'(T_1) - 2i\hat{\xi}_e \omega_e^2 b(T_1) \\ &\quad + \hat{m}_e a(T_1)\omega^2 \exp(-i\sigma_1 T_1) \\ &\quad - \hat{c}_e i\omega a(T_1)\exp(-i\sigma_1 T_1) = 0 \end{aligned} \tag{25}$$

To simplify Eqs. (24) and (25), we should set:

$$a(T_1) = \frac{1}{2}A(T_1)\exp(i\phi(T_1)) \tag{26}$$

$$b(T_1) = \frac{1}{2}B(T_1)\exp(i\psi(T_1)) \tag{27}$$

Substituting Eqs. (26) and (27) into Eqs. (24) and (25), we obtain:

$$\begin{aligned} &-2i\omega[A'(T_1) + iA(T_1)\phi'(T_1)] - 2\hat{\zeta} i\omega^2 A(T_1) \\ &\quad - \frac{3}{4}\hat{a}_1 A^3(T_1) - \frac{5}{8}\hat{a}_2 A^5(T_1) \\ &\quad + \hat{\theta} B(T_1)\exp(i\Theta(T_1)) - i\hat{f}\exp(i\Phi(T_1)) = 0 \end{aligned} \tag{28}$$

$$\begin{aligned} &-i\omega_e \left[B'(T_1) + iB(T_1)\psi'(T_1)\right] - i\hat{\xi}_e \omega_e^2 B(T_1) \\ &\quad + \frac{1}{2}\hat{m}_e \omega^2 A(T_1)\exp(-i\Theta(T_1))) \\ &\quad - i\frac{1}{2}\hat{c}_e \omega A(T_1)\exp(-i\Theta(T_1))) = 0 \end{aligned} \tag{29}$$

where the new variables $\Phi(T_1) = \sigma T_1 - \phi(T_1)$ and $\Theta(T_1) = \sigma_1 T_1 + \psi(T_1) - \phi(T_1)$ are used.

Separating the real part from the imaginary part, it is easy to obtain:

$$2\omega A' + 2\hat{\zeta}\omega^2 A + \hat{f}\cos\Phi - \hat{\theta} B\sin\Theta = 0 \tag{30}$$

$$\begin{aligned} &2\omega\sigma A - 2\omega A\Phi' - \frac{3}{4}\hat{a}_1 A^3 \\ &\quad - \frac{5}{8}\hat{a}_2 A^5 + \hat{f}\sin\Phi + \hat{\theta} B\cos\Theta = 0 \end{aligned} \tag{31}$$

$$\begin{aligned} &2\omega_e B' + 2\hat{\zeta}_e \omega_e^2 B + \hat{m}_e \omega^2 A\sin\Theta \\ &\quad + \hat{c}_e \omega A\cos\Theta = 0 \end{aligned} \tag{32}$$

$$\begin{aligned} &2\omega_e(\Theta' - \Phi' + \sigma - \sigma_1)B + \hat{m}_e A\omega^2\cos\Theta \\ &\quad - \hat{c}_e A\omega\sin\Theta = 0 \end{aligned} \tag{33}$$

Considering the steady-state cases for $A' = 0.0$, $\Phi' = 0.0$, $B' = 0.0$, $\Theta' = 0.0$ and denoting them as A_0, Φ_0, B_0 and Θ_0, the following equations are obtained:

$$2\hat{\zeta}\omega^2 A_0 + \hat{f}\cos\Phi_0 - \hat{\theta} B_0\sin\Theta_0 = 0 \tag{34}$$

$$\begin{aligned} &2\omega\sigma A_0 - \frac{3}{4}\hat{a}_1 A_0^3 - \frac{5}{8}\hat{a}_2 A_0^5 \\ &\quad + \hat{f}\sin\Phi_0 + \hat{\theta} B_0\cos\Theta_0 = 0 \end{aligned} \tag{35}$$

$$\begin{aligned} &2\hat{\zeta}_e \omega_e^2 B_0 + \hat{m}_e \omega^2 A_0\sin\Theta_0 \\ &\quad + \hat{c}_e \omega A_0\cos\Theta_0 = 0 \end{aligned} \tag{36}$$

$$\begin{aligned} &2\omega_e(\sigma - \sigma_1)B_0 + \hat{m}_e \omega^2 A_0\cos\Theta_0 \\ &\quad - \hat{c}_e \omega A_0\sin\Theta_0 = 0 \end{aligned} \tag{37}$$

Above equations can be converted to:

$$(2\hat{\zeta}\omega^2 A_0 - \hat{\theta} B_0 \sin\Theta_0)^2 + \left(2\omega\sigma A_0 - \frac{3}{4}\hat{a}_1 A_0^3 - \frac{5}{8}\hat{a}_2 A_0^5 + \hat{\theta} B_0 \cos\Theta_0\right)^2 = \hat{f}^2 \quad (38)$$

$$2\hat{\zeta}_e\omega_e^2 B_0 + \hat{m}_e\omega^2 A_0 \sin\Theta_0 + \hat{c}_e\omega A\cos\Theta_0 = 0 \quad (39)$$

$$2\omega_e(\sigma - \sigma_1)B_0 + \hat{m}_e\omega^2 A_0\cos\Theta_0 - \hat{c}_e\omega A_0 \sin\Theta_0 = 0 \quad (40)$$

Thus, the following relationship can be derived:

$$\{[2\hat{\zeta}_e\omega_e^2\hat{c}_e\omega + 2\omega_e(\sigma-\sigma_1)\hat{m}_e\omega^2]^2 + [2\hat{\zeta}_e\omega_e^2\hat{m}_e\omega^2 - 2\omega_e(\sigma-\sigma_1)\hat{c}_e\omega]^2\}B_0^2 = (\hat{m}_e^2\omega^4 + c_e^2\omega^2)^2 A_0^2 \quad (41)$$

Furthermore, Eq. (41) is converted into:

$$\{2\hat{\zeta}\omega^2(\hat{m}_e^2\omega^4 + \hat{c}_e^2\omega^2)A_0^2 + \hat{\theta}[2\hat{\zeta}_e\omega_e^2\hat{m}_e\omega^2 - 2\omega_e(\sigma-\sigma_1)\hat{c}_e\omega]B_0^2\}^2 + \left\{\left(2\omega\sigma A_0 - \frac{3}{4}\hat{a}_1 A_0^3 - \frac{5}{8}\hat{a}_2 A_0^5\right)\times(\hat{m}_e^2\omega^4 + \hat{c}_e^2\omega^2)A_0 - \hat{\theta}\left[2\hat{\zeta}_e\omega_e^2\hat{c}_e\omega + 2\omega_e(\sigma-\sigma_1)\hat{m}_e\omega^2\right]B_0^2\right\}^2 = \hat{f}^2(\hat{m}_e^2\omega^4 + \hat{c}_e^2\omega^2)^2 A_0^2 \quad (42)$$

Therefore, the effective output voltage across R is:

$$\begin{aligned}\upsilon_R(T_0,T_1) &= \varepsilon\upsilon_{R0}(T_0,T_1) + \varepsilon^2\upsilon_{R1}(T_0,T_1)\\ &= -\frac{2\varepsilon\hat{\zeta}_e}{\omega_e}(D_0 + \varepsilon D_1 + \cdots)(\upsilon_0(T_0,T_1) + \varepsilon\upsilon_1(T_0,T_1))\\ &\quad - \frac{\varepsilon\hat{c}_e}{\omega_e^2}(D_0 + \varepsilon D_1 + \cdots)(x_0(T_0,T_1) + \varepsilon x_1(T_0,T_1))\end{aligned} \quad (43)$$

The first-order approximate solution of υ_R is derived as follows:

$$\upsilon_R(t) = 2\zeta_e B(\varepsilon t)\sin(\omega_e t + \psi(\varepsilon t)) + \frac{c_e}{\omega_e^2}\omega A(\varepsilon t)\sin(\omega t + \phi(\varepsilon t)) + O(\varepsilon^2) \quad (44)$$

3 Analytical solutions

To discuss the nonlinear dynamic characteristics of the TEH with the RL resonant circuit, the analytical results derived in Sect. 2 will be presented in the following text. The equivalent potential energy function of the TEH can be expressed as:

$$\begin{aligned}U(x) &= \frac{\omega^2}{2}x^2 + \frac{a_1}{4}x^4 + \frac{a_2}{6}x^6\\ &= \frac{\omega^2}{x_1^2x_2^2}\frac{x^6}{6} - \frac{\omega^2}{x_1^2x_2^2}(x_1^2 + x_2^2)\frac{x^4}{4} + \omega^2\frac{x^2}{2}\end{aligned} \quad (45)$$

Thus, the corresponding equivalent restoring force can be obtained as follows:

$$\begin{aligned}f_r(x) &= \frac{\omega^2}{x_1^2x_2^2}x(x-x_1)(x+x_1)(x-x_2)(x+x_2)\\ &= \frac{\omega^2}{x_1^2x_2^2}x^5 - \frac{\omega^2}{x_1^2x_2^2}(x_1^2 + x_2^2)x^3 + \omega^2 x\end{aligned} \quad (46)$$

The variation of the potential energy function $U(x)$ as a function of the variable x and the parameter x_1 in the cases of $x_2 = 2.0$ is shown in Fig. 2. Under certain x_1 or x_2, the effect of x_2 or x_1 on the potential energy is consistent; thus, the other case will not be plotted again. It is found that the shape of potential energy wells with different x_1 is different. In Fig. 2b, the potential well depth of the TEH in the case of $x_1 = 1.2$ and $x_2 = 2.0$ is lowest among the four cases. Thus, the corresponding parameters a_1 and a_2 are calculated as $a_1 \approx -0.9444$ and $a_2 \approx 0.1736$. The other system parameters of the TEH are defined as: $\zeta = 0.6$, $\omega = 1.0$, $\theta = 0.5$, $\zeta_e = 0.5$, $m_e = 0.1$, $c_e = 0.5$, $f = 3.0$. In each case, above parameter values are default, and the new value will be given if any of them is changed.

To verify the effectiveness of the method of multiple scales, the numerical displacement amplitude and output voltage amplitude versus the excitation frequency are constructed by using the fourth-order Runge–Kutta algorithm. In numerical simulations, the relationships $A_0^2 = x^2 + \frac{\dot{x}^2}{\omega^2}$ and $B_0^2 = \upsilon^2 + \frac{\dot{\upsilon}^2}{\omega_e^2}$ are used. Several cases are plotted in Fig. 3, the approximate analytical results derived by Eq. (42) are depicted in solid lines and the numerical results are given in circles. It can be seen that a good agreement can be found between numerical simulations and analytical solutions.

In the following part, the effects of the system parameters on the displacement amplitude A_0 and the output voltage amplitude B_0 will be discussed.

Firstly, without the existence of the electromechanical coupling coefficient term ($\theta = 0$), the output voltage will not be discussed. As shown in Fig. 4, the displacement amplitude of the TEH for $\theta = 0$ is the traditional mechanical response curve (the dotted line in Fig. 4). Along with the increase of θ, the interesting

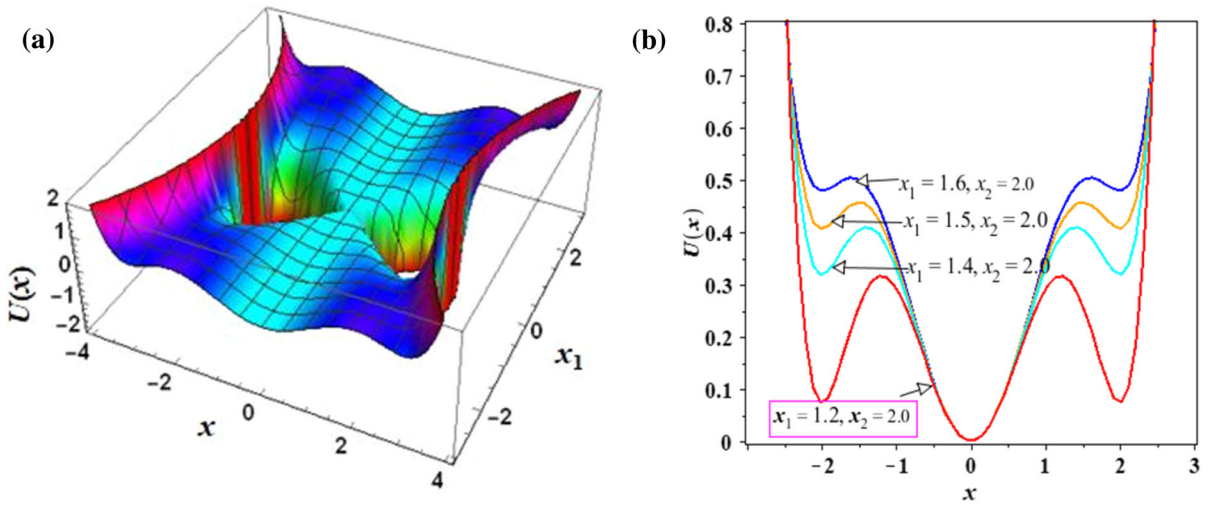

Fig. 2 **a** 3D surface of the potential energy function $U(x)$ with the variation in x and x_1; **b** potential energy function $U(x)$ with the variation in x for various sets of parameters x_1 and x_2

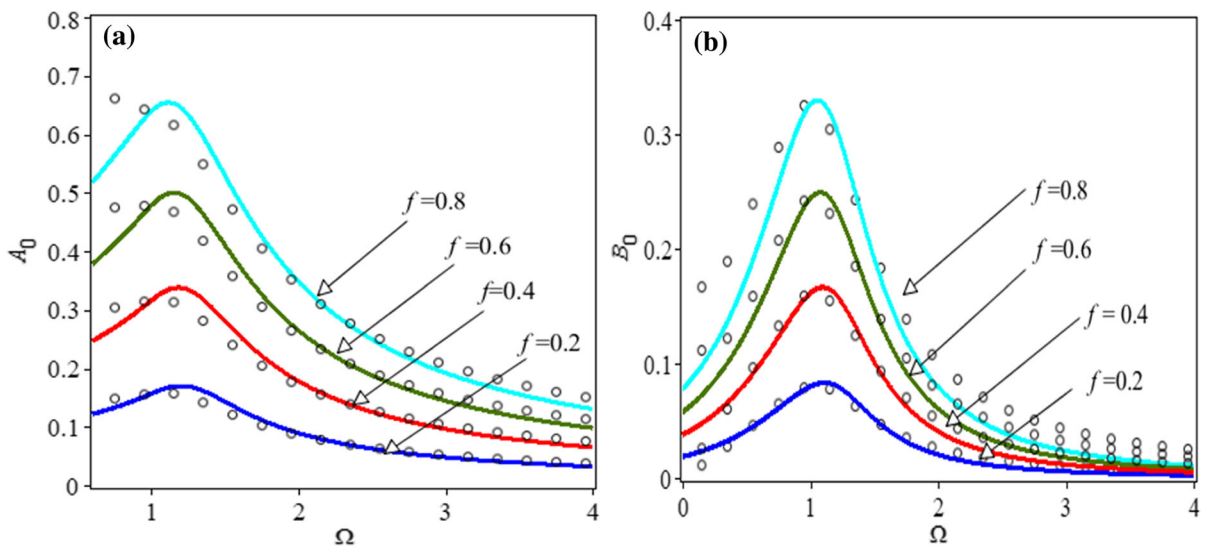

Fig. 3 Response of the system with the variation in excitation frequency Ω: **a** displacement amplitude A_0; **b** output voltage amplitude B_0

phenomenon can be observed. When θ is very small, the response curve is one continuous curve with a single peak as indicated in Fig. 4a. Then, the increase in the value of θ leads to the appearance of one small peak at the right side which can be seen in Fig. 4b at Point **P**. Further, the amplitude of the small peak will become higher (Point **Q** in Fig. 4c); meanwhile, one closed loop appears above the response curve in Fig. 4c, which is the phenomenon of frequency island. This kind of phenomenon also can be observed in Fig. 4d–f. The size of the island becomes larger.

Finally, the increase in the height of the right peak attaches to the island part, as depicted in Fig. 4g for the case of $\theta = 4.7$. Then, the displacement amplitude from two independent parts becomes one continuous curve with two peaks, such as the case of $\theta = 5.5$ in Fig. 4h. And the jump phenomenon can be observed in the right branch with increasing excitation frequency Ω. Then, increasing θ results in the right

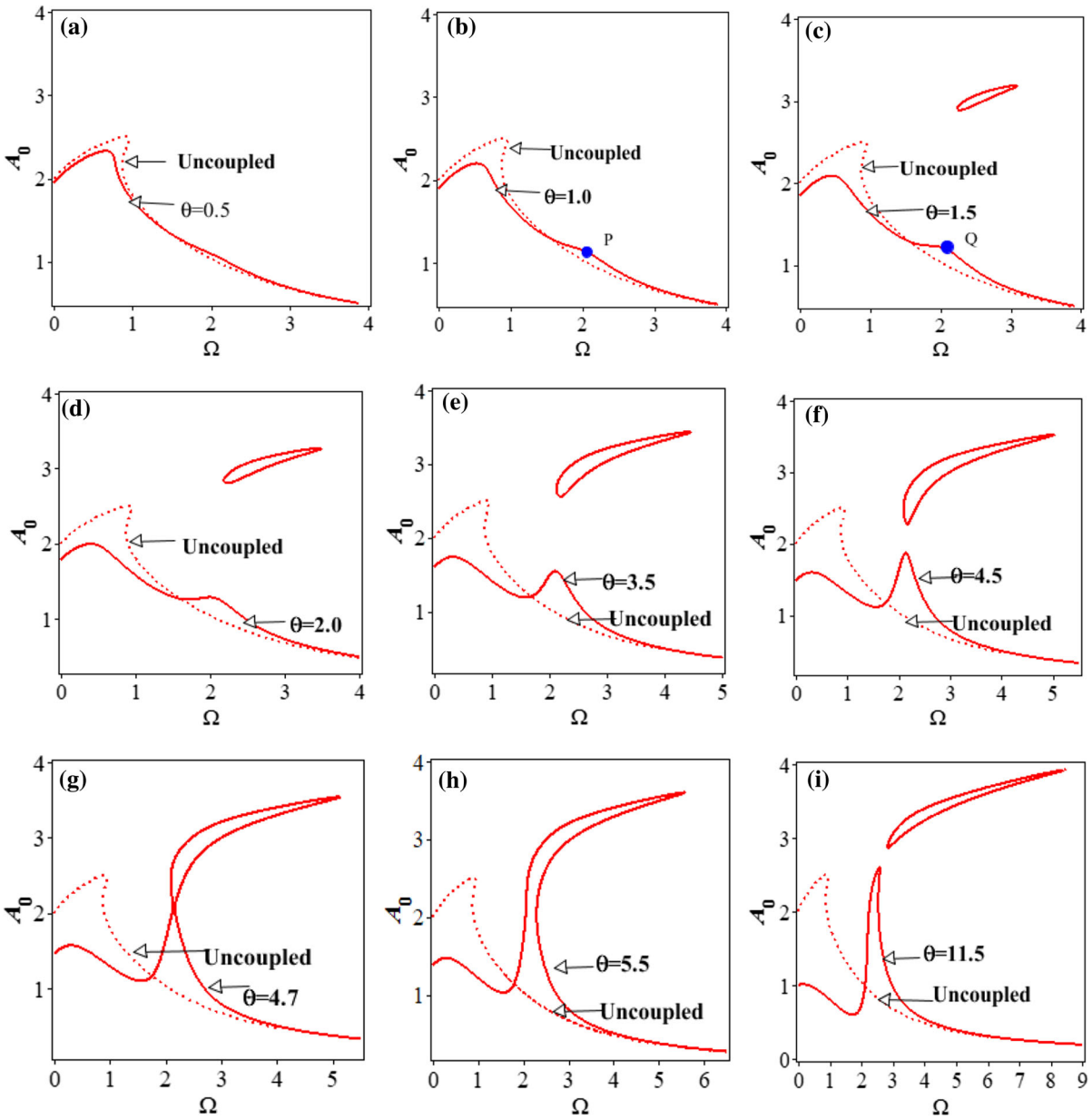

Fig. 4 Displacement amplitude A_0 with the variation in excitation frequency Ω under different electromechanical coupling coefficients θ: **a** $\theta = 0.5$; **b** $\theta = 1.0$; **c** $\theta = 1.5$; **d** $\theta = 2.0$; **e** $\theta = 3.5$; **f** $\theta = 4.5$; **g** $\theta = 4.7$; **h** $\theta = 5.5$; **i** $\theta = 11.5$. Note that 'Uncoupled' means $\theta = 0$

branch degenerating to the original frequency island and the continuous curve being below the island, as shown in Fig. 4i for the case of $\theta = 11.5$. The larger value of θ will lead to the lower displacement amplitude. In other words, the generated electric energy is transformed from mechanical energy of the TEH. The mechanical displacement will be suppressed if some mechanical energy is extracted. Thus, the variation in θ leads to the different dynamic response which must induce different characteristics of the output voltage. This will be discussed in Fig. 5.

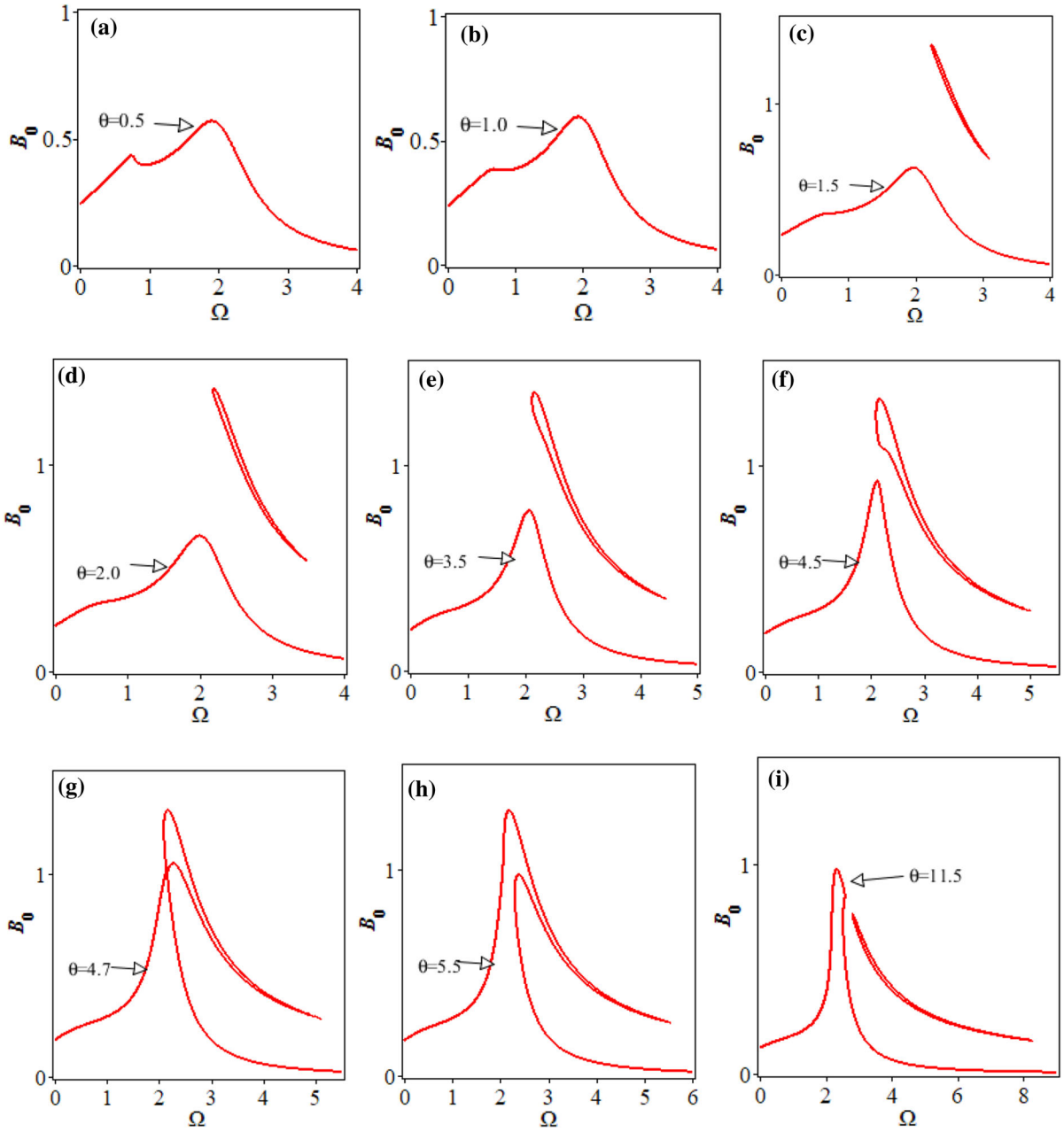

Fig. 5 Output voltage amplitude B_0 with the variation in excitation frequency Ω under different electromechanical coupling coefficients θ: **a** $\theta = 0.5$; **b** $\theta = 1.0$; **c** $\theta = 1.5$; **d** $\theta = 2.0$; **e** $\theta = 3.5$; **f** $\theta = 4.5$; **g** $\theta = 4.7$; **h** $\theta = 5.5$; **i** $\theta = 11.5$

Although the output voltage amplitude B_0 depends on the response displacement amplitude A_0, different response properties are indicated in Fig. 5. In the limit of small θ, the curve of output voltage amplitude B_0 is one independent branch, as shown in Fig. 5a, b. With the increase in θ, the peak value of output voltage amplitude B_0 also becomes larger. Meanwhile, the original curve is separated into two branches, which is also similar to the phenomenon of frequency island, as the cases indicated in Fig. 5c–f. The size of the island part becomes larger with the increase in θ; finally, the two branches attach to each other at the critical case

$\theta = 4.7$, which can be seen in Fig. 5g. Then, the curve of output voltage amplitude degenerates to one continuous curve, such as the case of $\theta = 5.5$ in Fig. 5h. The peak value still almost remains unchanged. However, when θ is too large, the peak value of B_0 decreases gradually, and meanwhile the phenomenon of frequency island is induced, which can be seen in Fig. 5i. This conclusion is the same as that from nonlinear energy harvesters with a pure load resistance [2]. Thus, the selection of the electromechanical coupling coefficient θ is important for improving the efficiency of the energy harvester.

Then, the effect of ω_e on the output voltage amplitude B_0 of the TEH with the RL resonant circuit is shown in Fig. 6a. Along with the variation of the detuning parameters Ω and ω_e, the change of the output voltage amplitude B_0 is shown in Fig. 6b. From the 3D plot, it can be found that with a small value of ω_e, two peaks could be found in the curve of output voltage amplitude B_0. Specifically, reducing the value of ω_e improves the level of output voltage amplitude B_0, as shown in Fig. 6a. For a larger value of ω_e, the curve of output voltage amplitude B_0 has one peak in the case of $\omega_e = 2.8$ as shown in Fig. 6a. Meanwhile, decreasing the value of ω_e makes the output voltage curve tend to show the other peak, such as the cases of $\omega_e = 1.5$ and $\omega_e = 1.2$ in Fig. 6a. Further, the height of the new peak increases gradually, and the value of this peak on the right side is greater than the peak on the left side at last, which can be seen clearly from the case of $\omega_e = 1.0$ in Fig. 6a.

Correspondingly, the direct result by numerical simulation for $\Omega = 1.5$ is plotted in Fig. 7 to verify the result in Fig. 6. The time histories of voltage $\upsilon(t)$ for the cases of $\omega_e = 1.0$, $\omega_e = 1.5$, $\omega_e = 2.0$, $\omega_e = 2.8$ are plotted, respectively. It can be seen that the maximum value of $\upsilon(t)$ decreases with the increase in ω_e, which is consistent with the results in Fig. 6a.

Furthermore, the dependence of the output voltage amplitude B_0 on the damping coefficient ζ_e is examined. The corresponding results are shown in Fig. 8. The increase in damping coefficient ζ_e induces the similar phenomenon as shown in Fig. 6, except that the frequency island phenomenon appears above on the response curve, as shown in Fig. 8b. For a small damping coefficient ζ_e, the output voltage amplitude B_0 usually will become large. However, the variation is obvious near to the right peak of the curve of output voltage amplitude B_0, which can be seen from Fig. 8b. And when the damping coefficient ζ_e is smaller, the frequency island phenomenon can be observed on the response curve of the output voltage amplitude, such as the case for $\zeta_e = 0.2$ in Fig. 8a. However, combining with the phenomena in Fig. 8a, it can be found that the

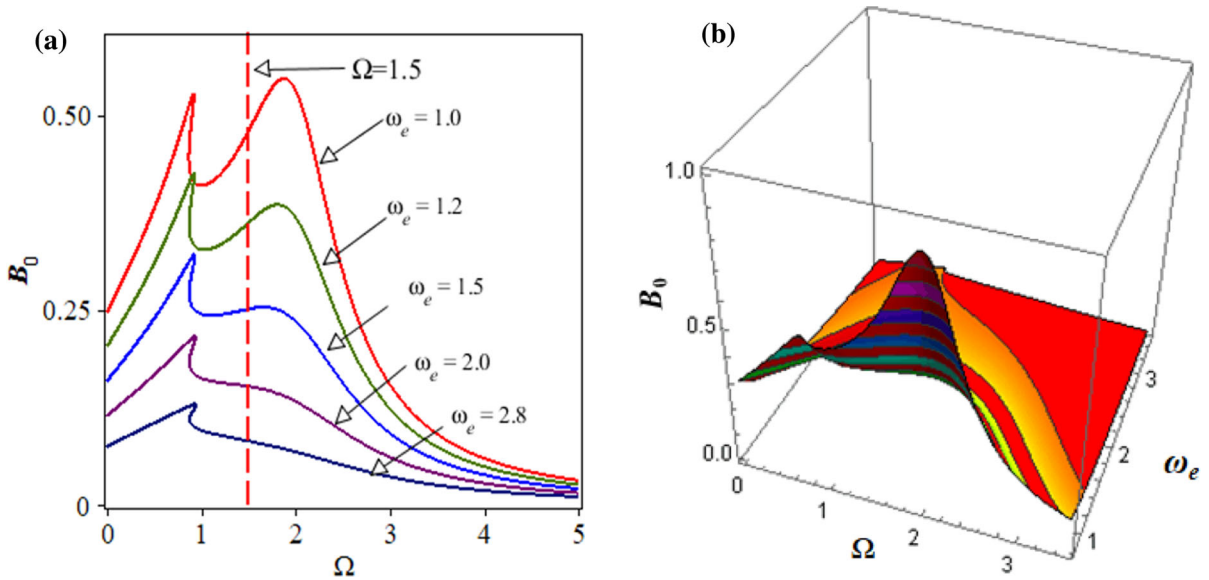

Fig. 6 **a** Output voltage amplitude with the variation in excitation frequency Ω under different values of ω_e, **b** 3D response surface of the output voltage amplitude with the variation in Ω and ω_e

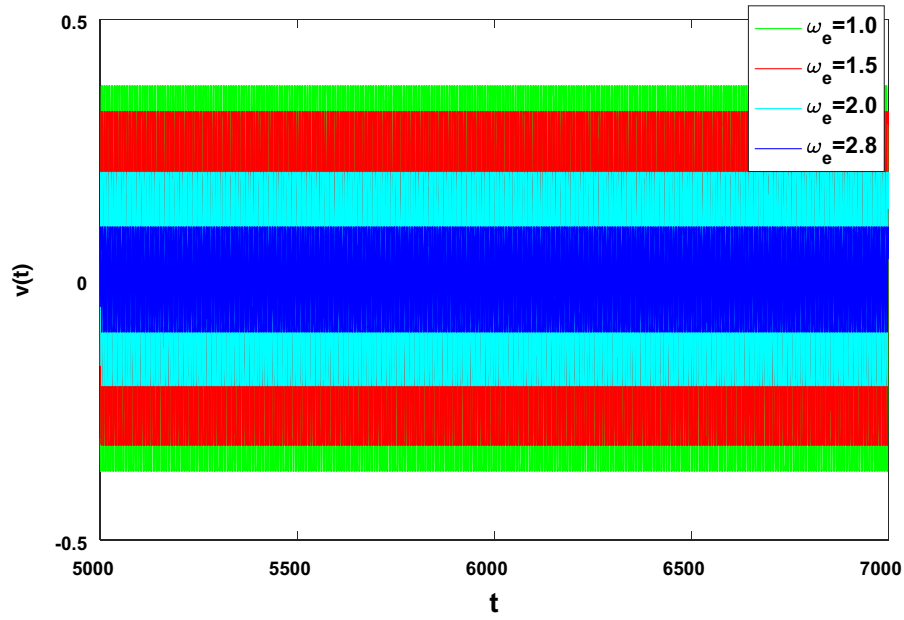

Fig. 7 Time histories of voltage $\upsilon(t)$ for $\omega_e = 1.0$, $\omega_e = 1.5$, $\omega_e = 2.0$ and $\omega_e = 2.8$ in the case of $\Omega = 1.5$

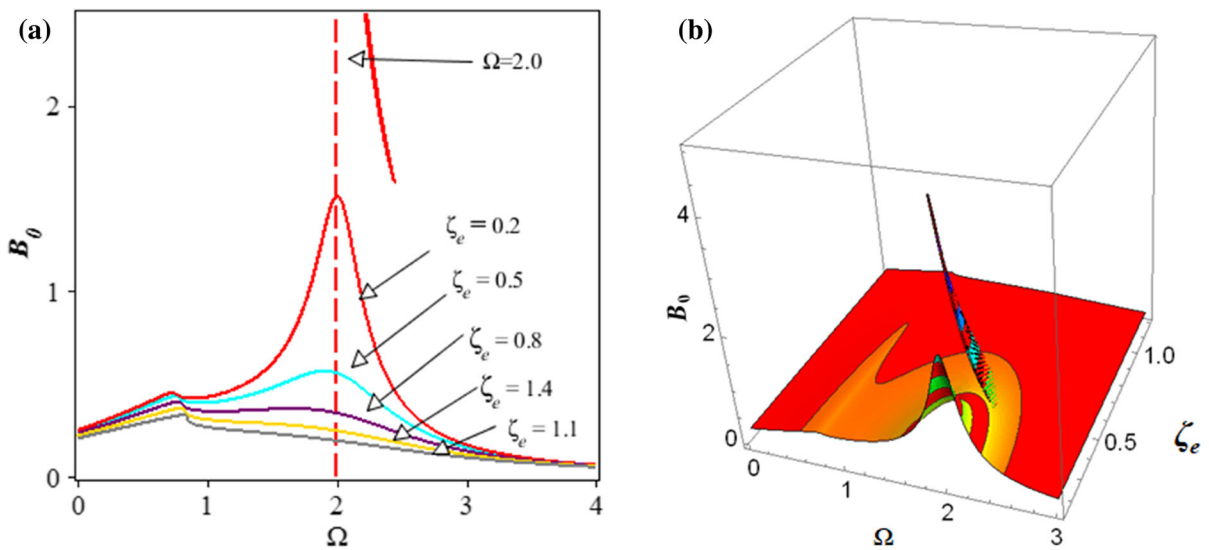

Fig. 8 **a** Output voltage amplitude with the variation in excitation frequency Ω under different values of damping coefficient ζ_e; **b** 3D response surface of the output voltage amplitude with the variation in excitation frequency Ω and damping coefficient ζ_e

effect on the left peak is weak. Thus, the appropriate choice of the damping coefficient ζ_e is important for improving the output voltage. Therefore, one certain ζ_e has an optimal excitation frequency for maximizing the output voltage of the TEH with the RL resonant circuit.

Then, the time histories of voltage $\upsilon(t)$ are plotted in Fig. 9 for $\Omega = 2.0$ to verify the results in Fig. 8. As can be seen that in Fig. 9 for the cases of $\zeta_e = 0.2$, $\zeta_e = 0.5$, $\zeta_e = 0.8$, $\zeta_e = 1.1$ and $\zeta_e = 1.4$, the maximum value of $\upsilon(t)$ decreases with the increase of the damping ζ_e, which is consistent with the results in Fig. 8a.

Under certain value of electromechanical coupling coefficient θ, the displacement amplitude and the output voltage amplitude versus the excitation amplitude f and frequency Ω are plotted in Fig. 10. The interesting

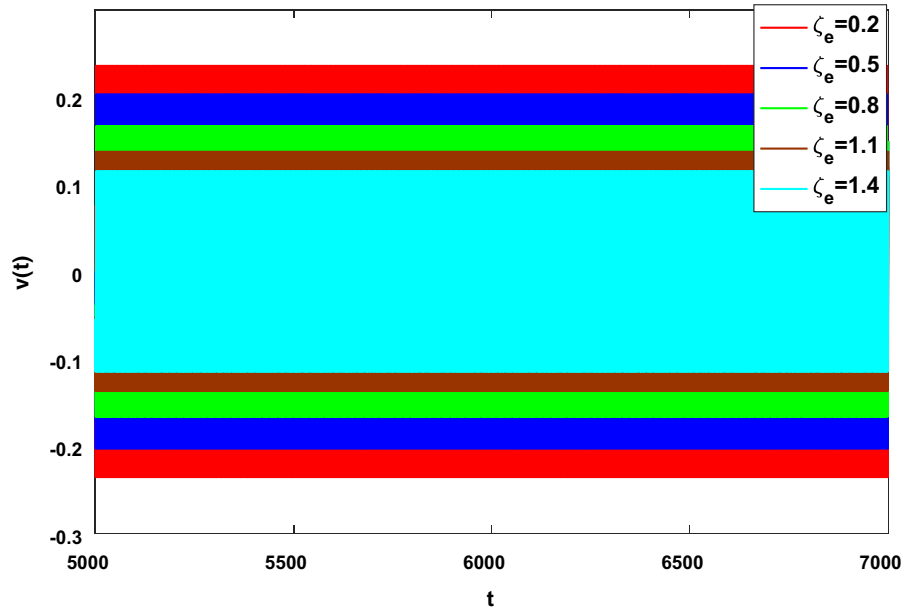

Fig. 9 Time histories of voltage $\upsilon(t)$ for $\zeta_e = 0.2$, ζ_e=0.5, $\zeta_e = 0.8$, $\zeta_e = 1.1$ and $\zeta_e = 1.4$ in the case of $\Omega = 2.0$

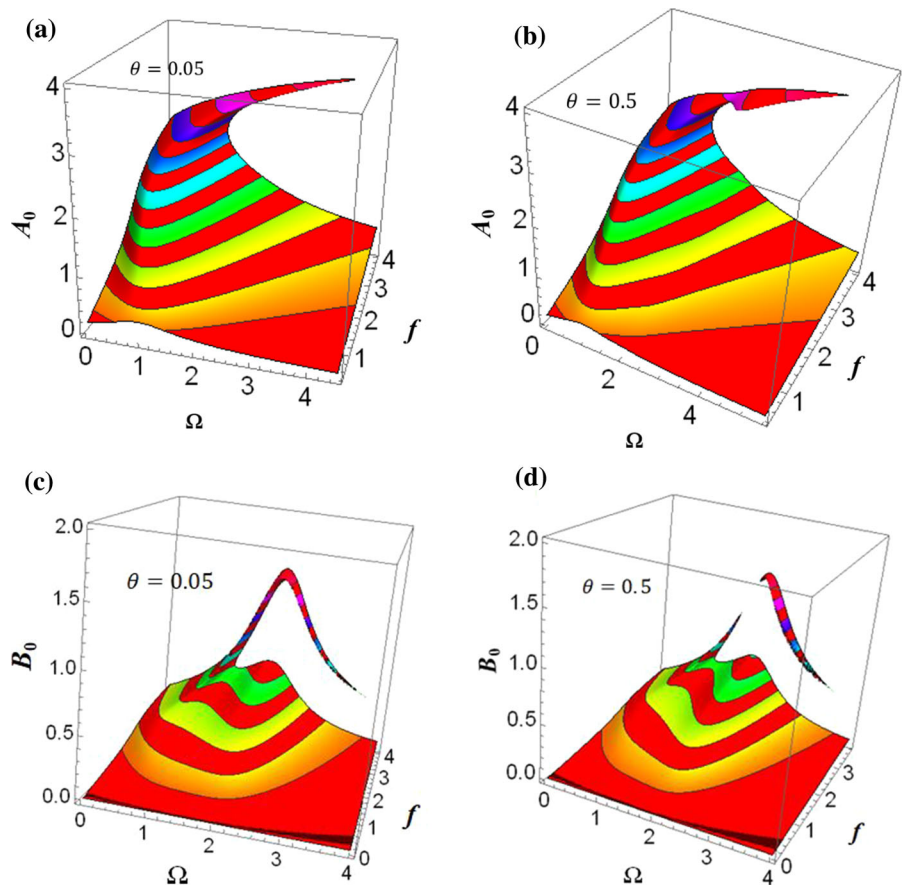

Fig. 10 3D response surface of the system with the variation in the excitation amplitude f and frequency Ω: **a** displacement amplitude for $\theta = 0.05$; **b** displacement amplitude for $\theta = 0.5$; **c** output voltage amplitude for $\theta = 0.05$; **d** output voltage amplitude for $\theta = 0.5$

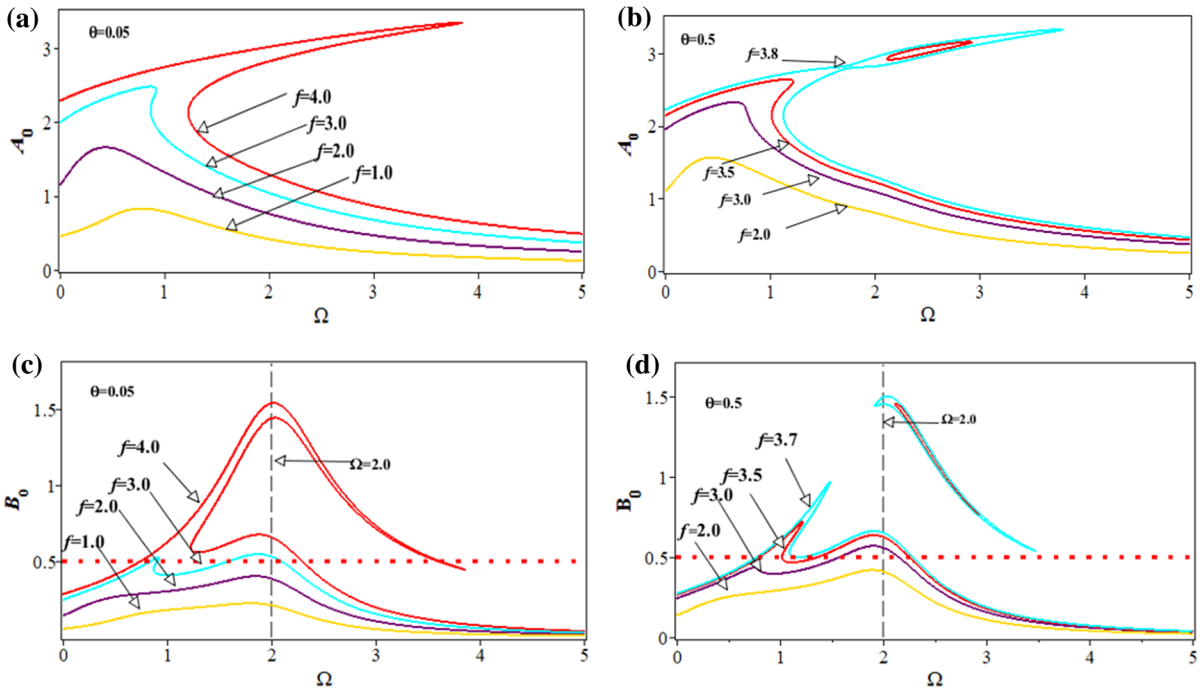

Fig. 11 Response of the system with the variation in Ω under different excitation amplitudes f. **a** Displacement amplitude A_0 for $\theta = 0.05$; **b** Displacement amplitude A_0 for $\theta = 0.5$; **c** output voltage amplitude B_0 for $\theta = 0.05$; **d** output voltage amplitude B_0 for $\theta = 0.5$

phenomenon can be found. For $\theta = 0.05$, the displacement amplitude A_0 bends to the higher frequency direction; however, the part of displacement amplitude A_0 which tends to the higher frequency direction shows the novel phenomenon for $\theta = 0.5$. This also leads to the separation of output voltage amplitude into two parts as depicted in Fig. 10d, actually, which is also induced by the appearance of frequency island phenomenon.

In order to further discuss the response phenomenon in Fig. 10, several values of the excitation amplitude f are selected, and the corresponding displacement amplitudes and the output voltage amplitudes of the TEH with the RL resonant circuit under different excitation amplitudes are calculated in Fig. 11. Naturally, the increase of f improves the input energy and the corresponding output voltage will increase. It can be found from Fig. 11a that increasing f results in the response property from the traditional response curve becoming the response with jump phenomenon for the case of $\theta = 0.05$. When $\theta = 0.5$, the existence of the frequency island phenomenon with the increase in the excitation amplitude could be observed, such as $f = 3.5$; further, the two branches (continuous curve and frequency island) are attached to each other ($f = 3.8$ in Fig. 11b), and finally, the curve of displacement amplitude reverts to the original continuous curve.

Correspondingly, the novel phenomenon also appears at the output voltage curve as shown in Fig. 11c, d. The peak value of the output voltage amplitude B_0 on the left side increases quickly along with the increase in the excitation frequency for the case of $f = 4.0$. This peak reaches the highest point near to $\Omega = 2.0$. Finally, along with the increase in the excitation frequency, this branch decreases gradually, while the output voltage is greater than the other branch. For a larger value of θ, the similar phenomenon is observed. The difference is that the frequency island phenomenon appears above the main branch for a large value of f, such as the cases of $f = 3.5$ and $f = 3.7$ in Fig. 11d.

Furthermore, for verifying the analytical results in Fig. 11, the time histories for the case of $\Omega = 2.0$ and $\theta = 0.05$ are taken as an example, which are shown in Fig. 12. It could be seen that with the increase in the excitation amplitude f, the value of voltage $\upsilon(t)$ increases, which is the same as the response result in Fig. 11a.

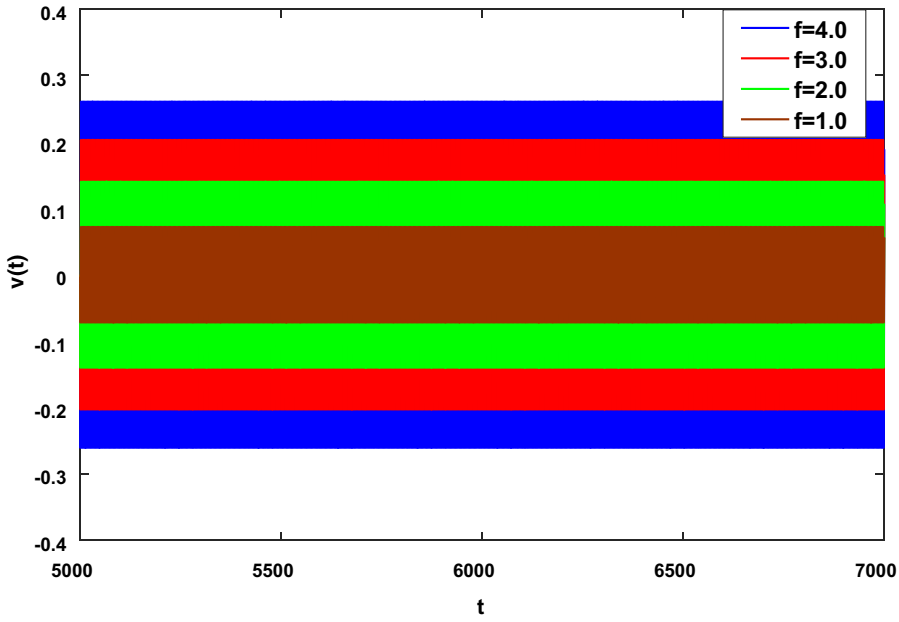

Fig. 12 Time histories of voltage $\upsilon(t)$ for $f = 1.0$, $f = 2.0$, $f = 3.0$ and $f = 4.0$ in the case of $\theta = 0.05$ and $\Omega = 2.0$

It can be found that the excitation amplitude f and electromechanical coupling coefficient θ are the utmost important factors for the output voltage. The selection of parameter pairs (f, θ) is considered for enhancing the energy harvesting performance of the TEH with the RL resonant circuit. For a considerably large output voltage, fixed here $B_{\max} = 0.5$, the selection of the parameter pairs (f, θ) is shown in Fig. 13. Above the critical line, under the corresponding values of (f, θ), the maximum output voltage is greater than 1.0, which can be verified from the results shown in Fig. 11. For the case of $f = 2.0$ in Fig. 11d, the maximum output voltage is smaller than 0.5, which can be found in Fig. 13 that point $\mathbf{P}_1$ lies below the critical line. For the cases of $f = 3.0$, $f = 3.5$ and $f = 3.7$, the maximum output voltage is greater than 0.5. As shown in Fig. 13, points $\mathbf{Q}_1$, $\mathbf{M}_1$ and $\mathbf{N}_1$ lie in the region satisfied $B_{\max} > 0.5$. For the case of $\theta = 0.05(f = 3.0$ and $f = 4.0)$, the corresponding output voltage is greater than 0.5 as shown in Fig. 11c. This is consistent with the results in Fig. 13, as points $\mathbf{M}_0$ and $\mathbf{N}_0$ are above the critical line. On the contrary, for the cases of $f = 1.0$ and $f = 2.0$, points $\mathbf{P}_0$ and $\mathbf{Q}_0$ are below the critical line, which can be found from Fig. 11c. That is the output voltage amplitude in these two cases is smaller than 0.5. Therefore, the parameter pairs which lie above the critical line are better for high-efficiency energy harvesting.

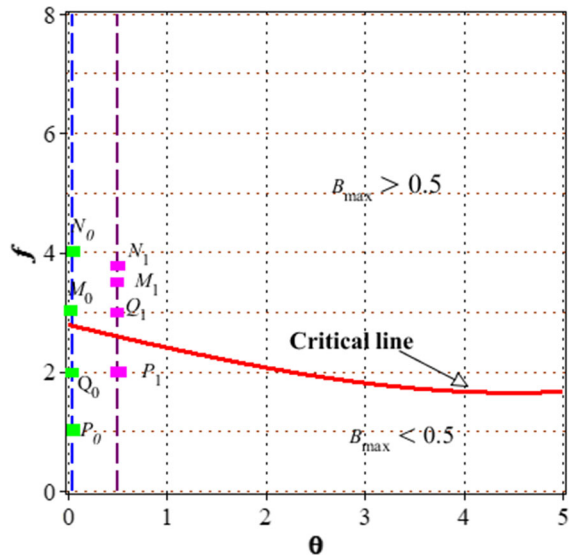

Fig. 13 Selection of the excitation amplitude f and electromechanical coupling coefficient θ. The critical line in red separates small (below the line) and large (above the line) voltage outputs. (Colour figure online)

Finally, the effect of the detuning parameter σ_1 on the displacement amplitude and the output voltage of the TEH with the RL resonant circuit is shown in Fig. 14. Note that the local minimum of the displacement amplitude A_0 appears approximately to $\Omega = 1.0$. The reason is that the detuning parameter σ_1 is zero. This viewpoint can be verified by examining the results

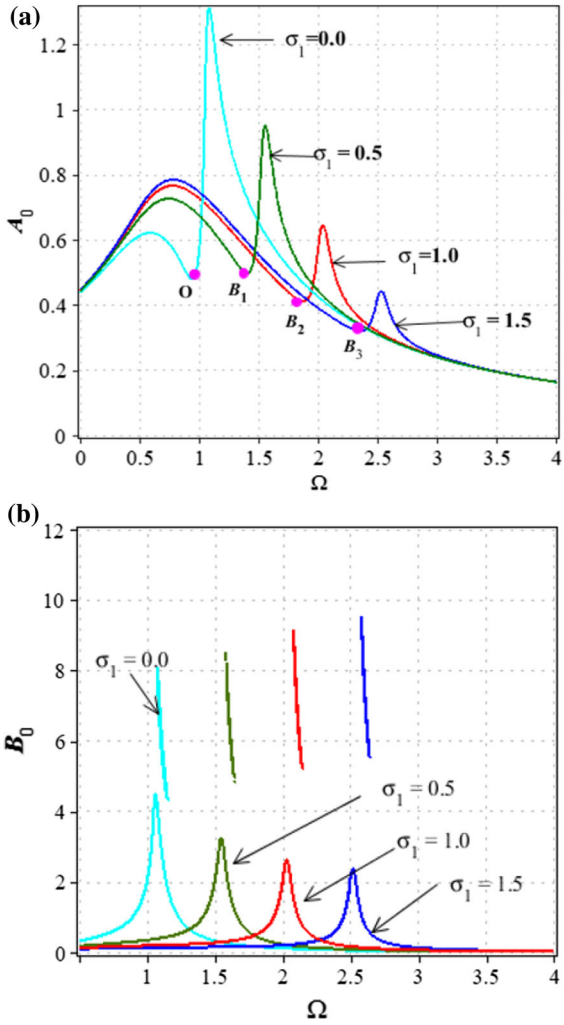

Fig. 14 Response of the system with the variation in Ω under different detuning parameters σ_1. **a** Displacement amplitude A_0; **b** output voltage amplitude B_0 ($\zeta = 0.6, \theta = 0.5, a_1 = -0.9444$, $a_2 = 0.1736$, $\zeta_e = 0.1$, $m_e = 0.1$, $c_e = 0.5$, $\sigma_1 = 1.0$ and $f = 1.0$)

in Fig. 14. With the variation in the value of σ_1, the critical point Ω for the appearance of the local minimum amplitude also increases. Correspondingly, the peak of A_0 reduces along with the increase in detuning parameter σ_1. However, the peak output voltage amplitude improves along with the increase of σ_1.

4 Conclusions

This paper presents a theoretical framework to analyze and predict the dynamic responses and the energy harvesting performance of the vibrational tristable energy harvester with a RL resonant circuit. Based on the method of multiple scales, the approximate analytical solutions of the steady-state displacement and output voltage are derived. Rich dynamic phenomena are induced by the variable parameters of the harvester. Results demonstrate that the excitation amplitude and the electromechanical coupling coefficient play significant roles for the energy harvesting performance. In addition, the selection of the parameter pairs (the excitation amplitude and the electromechanical coupling coefficient) is analyzed. Overall, the influence mechanism of the excitation conditions and the system parameters on the dynamic responses is revealed. In the future work, the optimization design of the both structural and electrical parameters of the tristable energy harvester will be performed.

Acknowledgements This work was supported by the National Natural Science Foundation of China (Grant Nos. 11702201, 11802237), China Postdoctoral Science Foundation (Grant No. 2018M641012), the Fundamental Research Funds for the Central Universities (Grant No. G2018KY0306) and Natural Science Basic Research Plan in Shaanxi Province of China (Grant No. 2018JQ1088).

References

1. Wei, C., Jing, X.: A comprehensive review on vibration energy harvesting: modelling and realization. Renew. Sustain. Energy Rev. **74**, 1–18 (2017)
2. Yang, Z., Zhou, S., Zu, J., Inman, D.J.: High-performance piezoelectric energy harvesters and their applications. Joule **2**, 642–697 (2018)
3. Mbong, T.D., Siewe, M.S., Tchawoua, C.: Controllable parametric excitation effect on linear and nonlinear vibrational resonances in the dynamics of a buckled beam. Commun. Nonlinear Sci. Numer. Simul. **54**, 377–388 (2018)
4. Zhou, S., Yan, B., Inman, D.J.: A novel nonlinear piezoelectric energy harvesting system based on linear-element coupling: design, modeling and dynamic analysis. Sensors **18**(5), 1492 (2018)
5. Zou, H., Zhang, W., Li, W., Hu, K., Wei, K., Peng, Z., Meng, G.: A broadband compressive-mode vibration energy harvester enhanced by magnetic force intervention approach. Appl. Phys. Lett. **110**(16), 163904 (2017)
6. Andò, B., Baglio, S., Maiorca, F., Trigona, C.: Analysis of two dimensional, wide-band, bistable vibration energy harvester. Sens. Actuators A Phys. **202**, 176–182 (2013)
7. Fang, Z., Zhang, Y., Li, X., Ding, H., Chen, L.: Integration of a nonlinear energy sink and a giant magnetostrictive energy harvester. J. Sound Vib. **391**, 35–49 (2017)
8. Cottone, F., Vocca, H., Gammaitoni, L.: Nonlinear energy harvesting. Phys. Rev. Lett. **102**(8), 080601 (2009)

9. Litak, G., Friswell, M.I., Adhikari, S.: Magnetopiezoelastic energy harvesting driven by random excitations. Appl. Phys. Lett. **96**(21), 214103 (2010)
10. Litak, G., Borowiec, M., Friswell, M.I., Adhikari, S.: Energy harvesting in a magnetopiezoelastic system driven by random excitations with uniform and Gaussian distributions. J. Theor. Appl. Mech. **49**(3), 757–764 (2011)
11. Erturk, A., Hoffmann, J., Inman, D.J.: A piezomagnetoelastic structure for broadband vibration energy harvesting. Appl. Phys. Lett. **94**(25), 254102 (2009)
12. Zhou, S., Cao, J., Erturk, A., Lin, J.: Enhanced broadband piezoelectric energy harvesting using rotatable magnets. Appl. Phys. Lett. **102**(17), 173901 (2013)
13. Stanton, S.C., McGehee, C.C., Mann, B.P.: Nonlinear dynamics for broadband energy harvesting: investigation of a bistable piezoelectric inertial generator. Phys. D **239**(10), 640–653 (2010)
14. Fotsa, R.T., Woafo, P.: Chaos in a new bistable rotating electromechanical system. Chaos Solit. Fract. **93**, 48–57 (2016)
15. Andò, B., Baglio, S., Maiorca, F., Trigona, C.: Analysis of two dimensional, wide-band, bistable vibration energy harvester. Sens. Actuators A Phys. **202**, 176–182 (2013)
16. Arrieta, A.F., Hagedorn, P., Erturk, A., Inman, D.J.: A piezoelectric bistable plate for nonlinear broadband energy harvesting. Appl. Phys. Lett. **97**(10), 104102 (2010)
17. Harne, R.L., Wang, K.W.: A review of the recent research on vibration energy harvesting via bistable systems. Smart Mater. Struct. **22**(2), 023001 (2013)
18. Daqaq, M.F., Masana, R., Erturk, A., Quinn, D.D.: On the role of nonlinearities in vibratory energy harvesting: a critical review and discussion. Appl. Mech. Rev. **66**(4), 040801 (2014)
19. Stanton, S.C., McGehee, C.C., Mann, B.P.: Reversible hysteresis for broadband magnetopiezoelastic energy harvesting. Appl. Phys. Lett. **95**(17), 174103 (2009)
20. Green, P.L., Worden, K., Atallah, K., Sims, N.D.: The benefits of Duffing-type nonlinearities and electrical optimisation of a mono-stable energy harvester under white Gaussian excitations. J. Sound Vib. **331**(20), 4504–4517 (2012)
21. Chen, L., Jiang, W.: Internal resonance energy harvesting. J. Appl. Mech. **82**, 031004 (2015)
22. Chen, L., Jiang, W., Panyam, M., Daqaq, M.F.: A broadband internally resonant vibratory energy harvester. J. Vib. Acoust. **138**, 061007 (2016)
23. Zhou, S., Cao, J., Inman, D.J., Lin, J., Liu, S., Wang, Z.: Broadband tristable energy harvester: modeling and experiment verification. Appl. Energy **133**, 33–39 (2014)
24. Kim, P., Seok, J.: Dynamic and energetic characteristics of a tri-stable magnetopiezoelastic energy harvester. Mech. Mach. Theory **94**, 41–63 (2015)
25. Li, H., Qin, W., Lan, C., Deng, W., Zhou, Z.: Dynamics and coherence resonance of tri-stable energy harvesting system. Smart Mater. Struct. **25**(1), 015001 (2016)
26. Tékam, G.T.O., Kwuimy, C.A.K., Woafo, P.: Analysis of tristable energy harvesting system having fractional order viscoelastic material. Chaos **25**(1), 013112 (2015)
27. Kwuimy, C.A.K., Litak, G., Nataraj, C.: Nonlinear analysis of energy harvesting systems with fractional order physical properties. Nonlinear Dyn. **80**(1–2), 491–501 (2015)
28. Panyam, M., Daqaq, M.F.: Characterizing the effective bandwidth of tri-stable energy harvesters. J. Sound Vib. **386**, 336–358 (2017)
29. Zhou, S., Zuo, L.: Nonlinear dynamic analysis of asymmetric tristable energy harvesters for enhanced energy harvesting. Commun. Nonlinear Sci. Numer. Simul. **61**, 271–284 (2018)
30. Zhou, S., Cao, J., Inman, D.J., Liu, S., Wang, W., Lin, J.: Impact-induced high-energy orbits of nonlinear energy harvesters. Appl. Phys. Lett. **106**(9), 093901 (2015)
31. Mallick, D., Amann, A., Roy, S.: Surfing the high energy output branch of nonlinear energy harvesters. Phys. Rev. Lett. **117**(19), 197701 (2016)
32. Lan, C., Tang, L., Qin, W.: Obtaining high-energy responses of nonlinear piezoelectric energy harvester by voltage impulse perturbations. Eur. Phys. J. Appl. Phys. **79**(2), 20902 (2017)
33. Syta, A., Litak, G., Friswell, M.I., Adhikari, S.: Multiple solutions and corresponding power output of a nonlinear bistable piezoelectric energy harvester. Eur. Phys. J. B **89**(4), 99 (2016)
34. HajiHosseinloo, A., Slotine, J.-J., Turitsyn, K.: Robust and adaptive control of coexisting attractors in nonlinear vibratory energy harvesters. J. Vib. Control (2017). https://doi.org/10.1177/1077546316688992
35. Yan, B., Zhou, S., Litak, G.: Nonlinear analysis of the tristable energy harvester with a resonant circuit for performance enhancement. Int. J. Bifurc. Chaos **28**(7), 1850092 (2018)
36. Erturk, A., Inman, D.J.: Piezoelectric energy harvesting. Wiley, Chichester, UK (2011)
37. Nayfeh, A.H., Mook, D.T.: Nonlinear oscillations. Wiley, Chichester (2008)
38. Huang, D., Zhou, S., Litak, G.: Theoretical analysis of multistable energy harvesters with high-order stiffness terms. Commun. Nonlinear Sci. Numer. Simul. **69**, 270–286 (2019)
39. Huang, D., Xu, W.: Performance characteristics of a real-power viscoelastic isolation system under delayed PPF control and base excitation. Nonlinear Dyn. **88**(3), 2035–2050 (2017)